Nanobody engineering for SARS-CoV-2 neutralization and detection

Liina Hannula[1], Suvi Kuivanen[2], Jonathan Lasham[3], Ravi Kant[2,4†], Lauri Kareinen[2,4†], Mariia Bogacheva[2], Tomas Strandin[4], Tarja Sironen[2,4], Vivek Sharma[1,3], Petri Saviranta[5], Anja Kipar[6,7], Olli Vapalahti[2,4,8], Juha T. Huiskonen[1] and Ilona Rissanen[1, *].

[1]*Institute of Biotechnology, Helsinki Institute of Life Science HiLIFE, University of Helsinki, Helsinki, Finland.*

[2]*Department of Virology, Medicum, Faculty of Medicine, University of Helsinki, Helsinki, Finland.*

[3]*Department of Physics, University of Helsinki, Helsinki, Finland.*

[4]*Departments of Veterinary Biosciences, University of Helsinki, Helsinki, Finland.*

[5]*VTT Technical Research Centre of Finland Ltd., FI-02044 VTT, Finland.*

[6]*Laboratory for Animal Model Pathology, Institute of Veterinary Pathology, Vetsuisse Faculty, University of Zurich, 8057 Zurich, Switzerland.*

[7]*Department of Infection Biology & Microbiomes, Institute of Infection, Veterinary and Ecological Sciences, University of Liverpool, Liverpool L3 3RF, UK.*

[8]*HUSLAB, Helsinki University Hospital, Helsinki, Finland.*

[†] Equal contributions

[*]Corresponding author

Keywords: SARS-CoV-2, nanobody, virus neutralization, neutralization escape

1   **Abstract**

2   In response to the ongoing SARS-CoV-2 pandemic, the quest for coronavirus inhibitors has

3   inspired research on a variety of small proteins beyond conventional antibodies, including

4   robust single-domain antibody fragments, 'nanobodies'. Here, we explore the potential of

5   nanobody engineering in the development of antivirals and diagnostic tools. Through fusion of

6   nanobody domains that target distinct binding sites, we engineered multimodular nanobody

7   constructs that neutralize wild-type SARS-CoV-2 and the Alpha and Delta variants with high

8   potency, with IC50 values up to 50 pM. However, we observed a limitation in the efficacy of

9   multimodular nanobodies against the Beta (B.1.351) and Omicron variants (B.1.1.529),

10   underlining the importance of accounting for antigenic drift in the design of biologics. To

11   further explore the applications of nanobody engineering in outbreak management, we present

12   a novel diagnostic assay, based on fusions of nanobodies with fragments of NanoLuc luciferase

13   that can detect sub-nanomolar quantities of the SARS-CoV-2 spike protein in a single step.

14   Our work showcases the potential of nanobody engineering to combat emerging infectious

15   disease.

16

17   **Introduction**

18   Antibody-based products comprise some of the most successful diagnostic and therapeutic

19   tools developed for managing the COVID-19 pandemic, ranging from at-home rapid antigen

20   tests for SARS-CoV-2 infection (*1, 2*) to neutralizing monoclonal antibodies (mAbs) used to

21   treat COVID-19 in individuals at risk of severe disease (*2, 3*). Neutralizing antibodies against

22   SARS-CoV-2 primarily target the Spike (S) protein (*4, 5*), a glycoprotein that mediates host-

23   cell recognition and viral entry (*6*). SARS-CoV-2 spikes are homotrimers, with each S chain

24   consisting of receptor-binding (S1) and fusogenic (S2) subunits (*7*). The S1 subunit contains

25 the receptor-binding domain (RBD) which mediates binding to the primary cellular receptor of

26 SARS-CoV-2, angiotensin-converting enzyme 2 (ACE2) (*6, 8, 9*). Following receptor binding,

27 the S2 subunit, a class I fusion protein, is activated by proteolytic cleavage and mediates the

28 fusion of the viral and cell membranes, delivering viral RNA to the cytoplasm (*8, 10*).

29 Due to its key role in initiating infection, the SARS-CoV-2 spike is the primary target of both

30 vaccines (*11*) and monoclonal antibody therapy (*2*). The continued efficacy of these powerful

31 approaches is challenged by the emergence of SARS-CoV-2 variants of concern (VOCs) that

32 display multiple amino acid substitutions in the S-protein (*12-14*). Following the spread of

33 variants Alpha (B.1.1.7), Beta (B.1.351) and Delta (B.1.617.2) (*15-20*), Omicron (B.1.1.529)

34 has become established as the dominant circulating variant in 2022, with new Omicron sub-

35 variants still emerging (*21*). VOC amino acid changes, including E484K found in Beta and

36 Omicron, can significantly reduce neutralization by antibodies raised against the 'wild-type'

37 SARS-CoV-2 (titled B.1 or Wuhan-Hu-1) (*12, 15, 16, 19, 22*). Current efforts to mitigate the

38 effects of immune escape on antibody-based COVID-19 countermeasures include the use of

39 antibody cocktails (*23, 24*) and the development of new antibody-based products, including

40 camelid single-domain antibody fragments ('nanobodies') (*25*).

41 In contrast to traditional mAbs, nanobodies are small (~15 kDa) and offer many advantages

42 including nebulized delivery and scalable, cost-effective production in bacterial expression

43 systems (*26, 27*). During the COVID-19 pandemic, antiviral nanobodies have garnered

44 significant interest, resulting in the discovery and structural characterization of several SARS-

45 CoV-2-neutralizing nanobodies (*27-37*). Furthermore, as nanobodies comprise self-contained

46 modules, they can be engineered into fusion proteins with enhanced properties. Pioneering

47 studies have started to chart the potential of engineered nanobodies as virus inhibitors (*38, 39*),

48 but their diagnostic applications are largely unexplored. While RT-qPCR remains the gold

49 standard for clinical diagnosis, rapid diagnostic tests designed to detect viral antigens with

3

50 conventional antibodies (*40*) are extensively applied in nonhospital settings. To our knowledge,

51 nanobodies have not, so far, been used for viral antigen detection in commercialized assays.

52 Here, we explore an engineering strategy that leverages nanobody fusions for enhanced

53 neutralization and in the development of a novel rapid-antigen assay. Tri-modular fusions of

54 selected nanobodies showed up to a hundredfold enhancement of the *in vitro* neutralization

55 efficiency against wild-type SARS-CoV-2 as compared to the reported efficiencies of the

56 single constituent nanobodies (*28-30, 41*). We suggest that molecular dynamics (MD)

57 simulations can be used to analyze the neutralization potential of nanobodies against VOCs, of

58 which Beta and Omicron escaped neutralization, and offer a possible mechanistic explanation

59 for the neutralization escape. Nanobody fusions were further engineered to produce proof-of-

60 concept for a novel diagnostic assay, which applies nanobodies fused to fragments of a split

61 signal molecule, NanoLuc luciferase (*42-44*), and allows the detection of picomolar

62 concentrations of SARS-CoV-2 spike protein in a single step. Overall, our study shows the

63 potential for engineered nanobodies as antiviral and diagnostic agents, which we envision can

64 offer affordable and scalable countermeasures during future outbreaks of emerging viral

65 diseases.

66

67 **Results**

68 **Structure-guided design of multimodular nanobodies.** Structural studies have elucidated

69 key sites of vulnerability on SARS-CoV-2 (*4, 45*), including an ACE2-receptor binding

70 interface that can be targeted to sterically hinder receptor engagement (*46-48*). Inspired by the

71 trimeric structure of the coronaviral spike (Figure 1), we sought to develop an approach for

72 targeting all three copies of RBD simultaneously to enhance SARS-CoV-2 inhibition.

73 Cryogenic electron microscopy (cryo-EM) studies have identified two distinct SARS-CoV-2

4

74   RBD conformations, titled 'up' and 'down' (*49, 50*), where putative epitopes on neighboring

75   RBDs are in proximity, within 40 to 74 Å from each other (SI Figure S1). To develop a tripartite

76   binder that could be sterically accommodated within these tight constraints, we selected

77   nanobodies, the smallest antibody-based protein inhibitors, as the base unit for

78   multimodularization.

79   We designed three trimodular nanobodies (Figure 1B) using the sequences of four previously

80   published monomeric nanobodies, Ty1 (*47*), H11-H4 (*29*), MR17-K99Y (*30*) and VHH V (*41*).

81   These modules were selected based on two criteria: (i) distinct epitope and angle of binding to

82   RBD (Figure 1C and SI Table S1), (ii) spatial proximity of the epitopes in the context of the

83   SARS-CoV-2 spike, facilitating the simultaneous binding of all modules (Figure 1). While each

84   individual module has been reported to neutralize wild-type SARS-CoV-2 with IC50 (half-

85   maximal inhibitory concentration) values ranging from 40 to 142 nM (SI Table S1), our

86   multimodularization approach was designed to improve neutralization potency through

87   increased avidity to the SARS-CoV-2 spike, and to test whether multimodular constructs can

88   neutralize variants of concern.

89   Multimodular nanobodies were constructed by fusing multiple nanobodies together with

90   flexible linkers of twenty amino acids (GGGGSx4) with the aim to improve the binding avidity

91   (*26, 39, 51-53*). Furthermore, as modules targeting distinct epitopes can be included in the same

92   construct, multimodularization has been proposed to reduce neutralization escape resulting

93   from amino acid changes in viral proteins (*41*). Here, construct compositions were selected to

94   test i) the effect of triplicating a single module (tri-Ty1, comprised of three Ty1 modules (*47*))

95   on SARS-CoV-2 neutralization, and ii) whether the inclusion of variable modules can help

96   mitigate neutralization escape by virus variants (*41*). To this end, multimodular constructs tri-

97   Ty1, tri-TMH, and tri-TMV (Figure 1B) were generated, with tri-TMH and tri-TMV comprised

98   of **T**y1 (*47*) and **M**R17-K99Y (*30*) modules, followed by either a **H**11-H4 (*29*) or VHH **V** (*41*)

99   module, respectively. Tri-Ty1, tri-TMH, and tri-TMV readily expressed in *E.coli*, and were

100 purified and enrolled in target binding and virus neutralization assays.

101
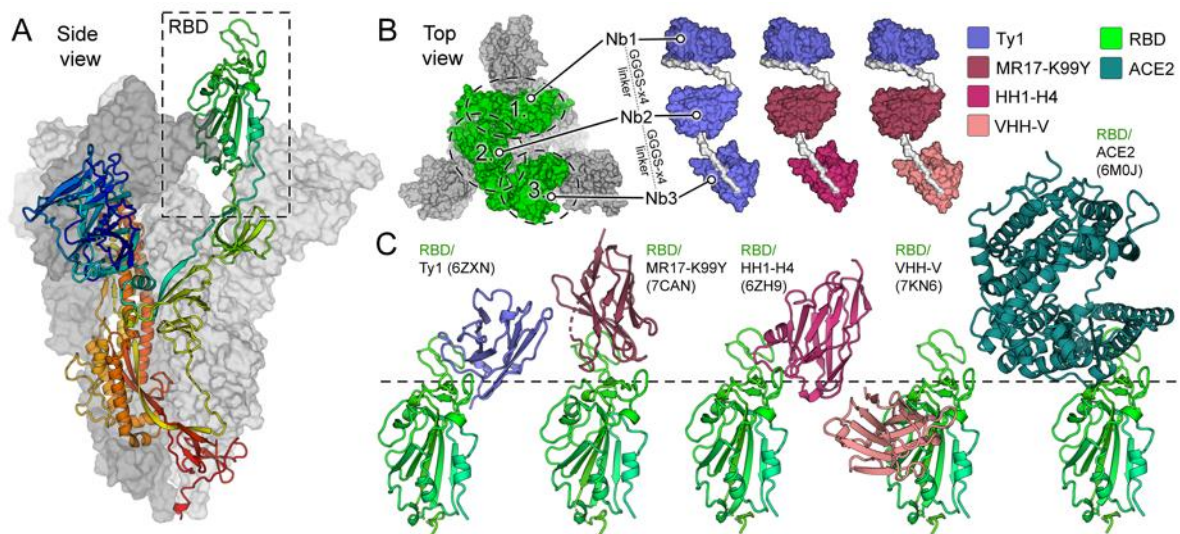
Figure 1. Structure-based design of multimodular nanobodies targeting SARS-CoV-2 S.
A) Side view of the SARS-CoV-2 S-trimer (*47*). One trimer subunit, with a receptor-binding
domain (RBD), in the 'up' conformation, is shown as a cartoon and colored as a rainbow
ramped from blue (N-terminus) to red (C-terminus). The two other subunits are shown as
surface representation in shades of grey. **B**) Three distinct multimodular nanobodies were
designed: (i) tri-Ty1 with three repeats of Ty1 (*47*) module; (ii) tri-TMH with Ty1, MR-17-
K99Y (*30*) and HH1-H4 (*29*) modules; and (iii) Tri-TMV with Ty1, MK and VHH-V (*41*)
modules. The nanobody modules are connected by flexible GGGGSx4 linkers. **C**) Each of the
nanobody domains (Ty1, MR17-K99Y, HH1-H4, and VHH-V) bind the RBD at a unique
angle. Comparison to the structure of RBD bound to the primary host-cell entry receptor of
SARS-CoV-2, ACE2 (*6, 54*) demonstrates that three of the modules bind epitopes proximal to
the ACE2-binding site, while VHH-V targets an alternative neutralization epitope.

114

Multimodular nanobodies bind variant forms of the RBD. Amino acid changes observed

in SARS-CoV-2 variants of concern have been linked to escape from antibody-mediated virus

neutralization (*15, 16, 55, 56*) due to reduced affinity to epitopes where key amino acids have

been altered. To determine how prominent RBD amino acid changes K417N, E484K, and

N501Y impact the binding of trimodular nanobodies, we tested their binding to RBD and spike

mutants in an antigen microarray. Nanobodies tri-Ty1, tri-TMH, and tri-TMV were tested

against (i) wild-type RBD, (ii-iv) three RBD variants that displayed either K417N, E484K, or

6

122 N501Y amino acid change, (v) wild-type S1 subunit, and (vi) a S1 subunit displaying the amino

123 acid changes K417N, E484K, N501Y, and D614G. Multimodular tri-TMH and tri-TMV

124 constructs contain nanobody modules that target three epitopes comprising a broad range of

125 residues, and as such, these constructs were expected to be less sensitive to amino acid changes

126 than the single-module tri-Ty1. The results support this hypothesis, showing that the binding

127 of tri-Ty1 to the RBD was strongly diminished by the E484K change, while this effect was

128 mitigated in tri-TMH and tri-TMV (Figure 2). Amino acid changes K417N or N501Y did not

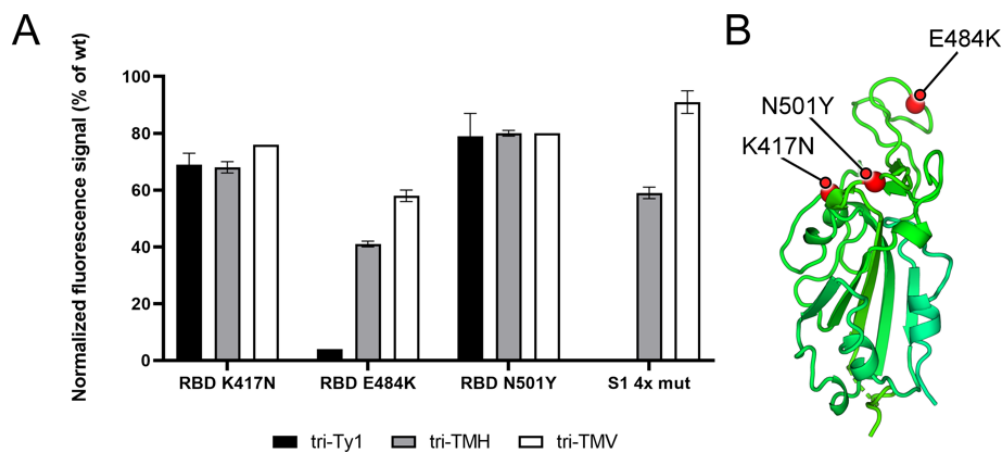129 significantly alter the binding affinity on any of the nanobody constructs.

Figure 2. Relative binding strength of trimeric nanobodies to different RBD and Spike S1 domain variants on the antigen microarray. A) Three multimodular nanobody constructs were tested in a binding array and were shown to bind different RBD or S1 domain variants. Binding of tri-Ty1 was obstructed by the amino acid change E484K, which is found in the Beta VOC and linked to neutralization escape (*12, 16, 55*) The multimodular nanobodies comprised of modules that target distinct epitopes, tri-TMH and tri-TMV, retained a level of binding to the E484K RBD variant. The fluorescence signals of Dylight 633-labelled trimeric nanobodies tri-Ty1, tri-TMH and tri-TMV bound to the different RBD and S1 mutants in the array were normalized relative to the corresponding wt protein signals in the same array. Error bars represent the standard deviation of two replicate wells. **B**) Location of the amino acid changes within the SARS-CoV-2 RBD in the Alpha and Beta variants. Amino acid change N501Y is found in the Alpha and Beta variants (*15, 16*), and the Beta variant displays the additional changes K417N and E484K (*16*).

7

153 **Multimodular nanobodies potently neutralize SARS-CoV-2 wild-type and Alpha.**

154 Multimodular nanobodies targeting SARS-CoV-2 S trimer were designed to increase

155 neutralization efficacy over single module nanobodies via enhanced avidity. In addition, the

156 ability of multimodular nanobodies to target distinct epitopes was expected to reduce

157 neutralization escape by emerging variants. To test these hypotheses, we determined the

158 neutralization potency of multimodular nanobodies against SARS-CoV-2 variants *in vitro*,

159 using a plaque-reduction neutralization assay in VeroE6-TMPRSS2 cells (Figure 3). All

160 multimodular nanobodies neutralized wild-type virus (50 pfu) at ultra-high potency, with IC50

161 values ranging from 160.9 pM for tri-Ty1, to 83.66 pM for tri-TMV and 50.11 pM for tri-TMH.

162 This result shows that the multimodular structure improves neutralization efficacy from the

163 single constituent nanobodies up to hundred-fold, which is in line with recent works presenting

164 similar, significant increase in neutralization potency over single module nanobodies (*38, 41,*

165 *57, 58*). Neutralization was also tested with virus administered at 1 MOI, where the relative

166 efficacies of the nanobodies followed the same trends as in the 50 pfu assay, although at

167 somewhat lower IC50-values ranging from 400 pM to 2 nM (SI Figure S5).

168 To investigate the capability of multimodular nanobodies to neutralize SARS-CoV-2 variants

169 of concern, we tested tri-TMH, the most potent neutralizer of wild-type SARS-CoV-2 among

170 our designs, against the wide-spread variants of concern Alpha, Beta, Delta, and Omicron. Tri-

171 TMH neutralizes SARS-CoV-2 Alpha variant with equivalent potency to wild-type (IC50 =

172 50.23 pM), and Delta with declined potency (estimated IC50 ~600 pM). The Beta and Omicron

173 variants, however, escaped neutralization by multimodular nanobodies (Figure 3B). We

174 hypothesize that the reduction of neutralization potency against Beta and Omicron arises from

175 the well-known neutralization escape mutation E484K, which is present in the Beta and

176 Omicron variants, but not in wild-type or the other variants studied. This contrasts with the

177 antigen microarray data (Figure 2), where nanobodies with three distinct modules were found

8

178   to retain most of their binding to RBD with this mutation. While neutralization is observed for

179   the Delta variant, the potency of tri-TMH against delta is reduced, presumably due to the other

180   changes in Delta, such as L452R, which has been linked to neutralization escape from

181   antibodies (*19, 59*).

182
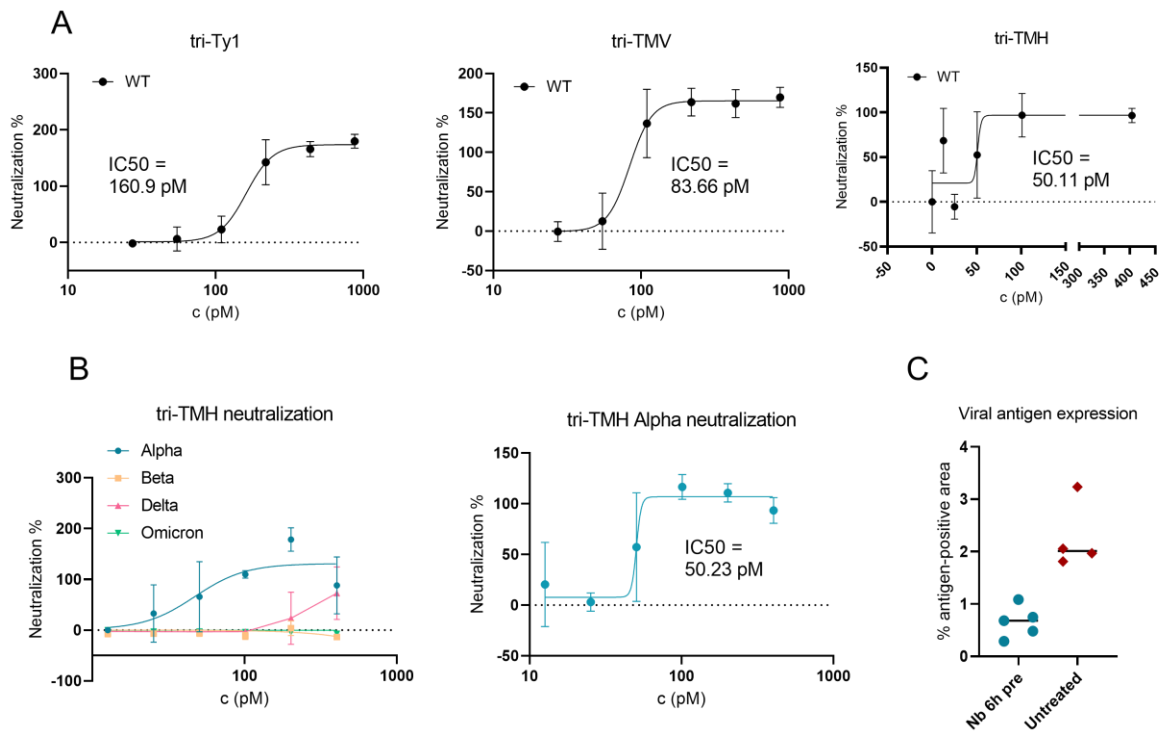
183 **Figure 3. Multimodular nanobodies neutralize SARS-CoV-2 wild-type, Alpha and Delta**

184 **variants at high potency and limit the course of the disease in a hamster model. A)** Wild-

185 type SARS-CoV-2 is neutralized by nanobodies tri-Ty1, tri-TMV, and tri-TMH. **B)** Tri-TMH

186 neutralizes the Alpha and Delta variants. **C)** A morphometric analysis of the presence of SARS-

187 CoV-2 antigens in lung tissue sections shows a decrease in viral antigen expression in hamsters

188 pre-treated with multimodular nanobody (Nb 6h pre), compared to untreated individuals (n =

189 5 in nanobody treated group, n = 4 in untreated).

190

191

192

193

194   **Cryo-EM analysis reveals the conformational landscape of SARS-CoV-2 spike bound to**

195   **a multimodular nanobody.** While many individual nanobody modules and their binding

196   epitopes on the S protein have been structurally characterized, these reconstructions may be

197   incommensurate to linker-connected multimodular nanobody constructs, as they do not

198   account for the potential steric constraints imposed by linker-bound modules (*29-37, 47*). As

199   such, the effects of multimodularity in S-targeting nanobodies on nanobody neutralization

200   mechanisms remain largely unexplored. We applied cryo-EM to determine the binding mode

201   of multimodular nanobody tri-TMH to SARS-CoV-2 S protein.

202   The receptor-binding domains of SARS-CoV-2 spike transition between states designated "up"

203   and "down", of which the "up" conformation is accessible to ACE2 receptor binding (*4, 7*).

204   This natural variation leads to the presence of distinct subpopulations in cryo-EM data, where

205   the conformational landscape is primarily comprised of fully closed ("all down") and partially

206   open ("2 down, 1 up") states (*4, 7, 60*). While differential distributions of the two states have

207   been reported, native spikes on viral surface show 31% and 55% of fully closed and partially

208   open conformations, respectively (*60*). Furthermore, certain neutralizing antibodies have been

209   shown to disrupt the conformation of the spike due to steric incompatibility with the prefusion

210   state (*61, 62*).

211   We set out to determine how nanobody tri-TMH impacts the conformation of the spike. Our

212   cryo-EM data showed that the spike retained a prefusion conformation with subpopulations

213   presenting the closed and partially open states. Both states are fully bound with tri-TMH

214   (Figure 4A), although due to the variable placement of the modules, local resolution does not

215   allow the unambiguous identification of individual nanobody moieties. Our results indicate that

216   the inclusion of multiple simultaneously binding modules, linked by the commonly used

217   (GGGGS)$_4$ linker, does not result in sufficient steric strain to disrupt the prefusion

218   conformation, and the linker seems to allow the native distribution of RBD conformational

10

219   states. We postulate that the increased potency of multimodular inhibitors is primarily derived

220   from enhanced avidity, as opposed to altered mechanistic properties.

221   **Molecular dynamics simulations indicate re-arrangement of nanobody-RBD interface as**

222   **a result of amino acid changes present in VOC.** Following the cryo-EM analysis that

223   validated the conformation of the spike and the RBDs, we sought to elucidate the molecular

224   basis for neutralization evasion as observed for VOC beta (Figure 3) via molecular dynamics

225   (MD) simulations. Interestingly, many nanobodies, as well as antibodies derived from B cells

226   of COVID-19 convalescent and vaccinated individuals, show a salt bridge between an antibody

227   scaffold arginine (R52 in nanobodies) and residue E484 of the RBD (*15, 16*). As this residue

228   is the site of amino acid change E484K that is linked to neutralization evasion by VOCs (*16,*

229   *22, 63*), we sought to determine how E484K impacts the interface of RBD and nanobody

230   modules included in tri-TMH. MD simulations of both WT RBD and E484K RBD were

231   performed with the individual nanobody module monomers.
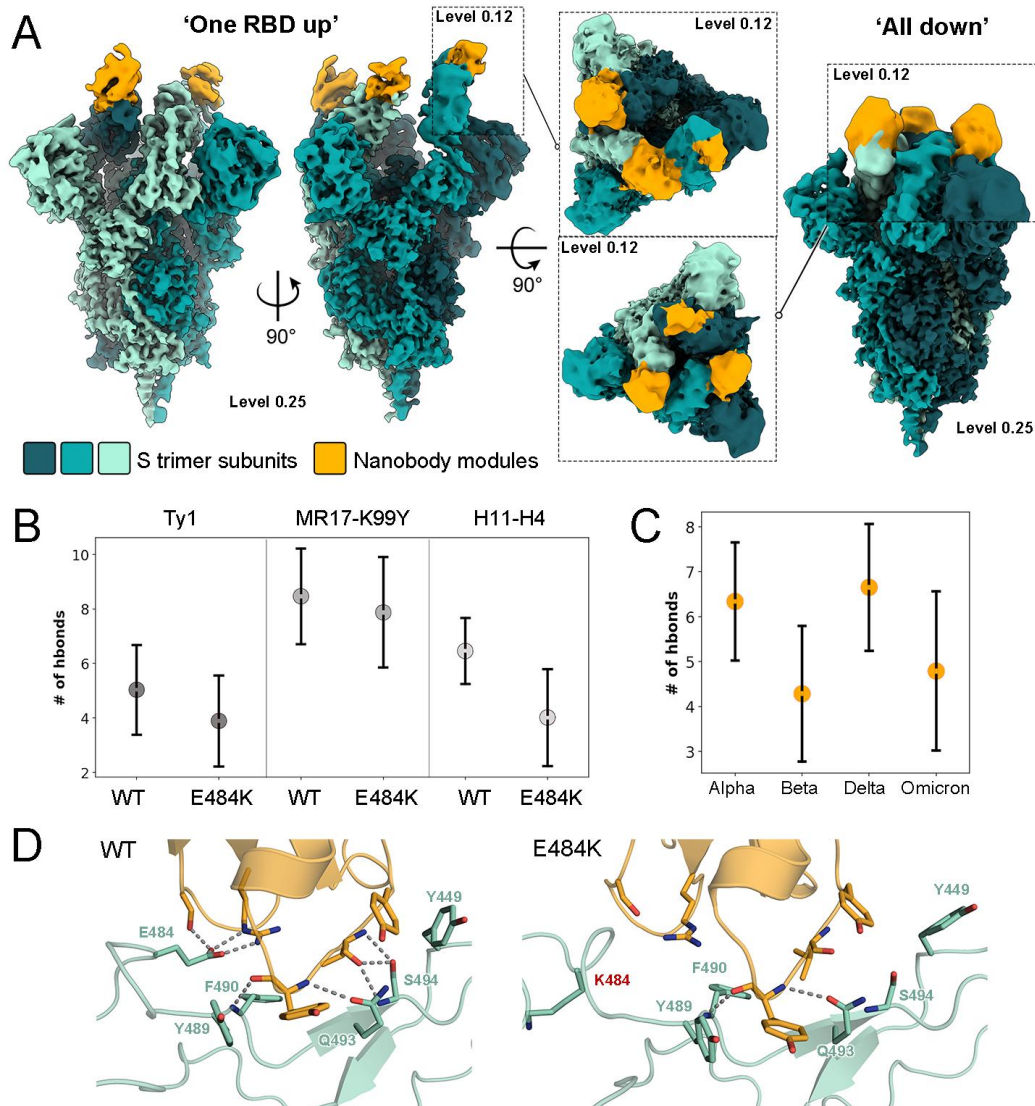
Figure 4. Insights into multimodular nanobody binding from cryo-EM analysis and molecular dynamics simulations. A) Cryo-EM reconstructions of the S-trimer with multimodular nanobody tri-TMH bound. The reconstructions show the typical spike protein conformations (one RBD up and all RBDs down). B) Number of hydrogen bonds between RBD (wild-type or with E484K amino acid change) and each nanobody module of tri-TMH observed from MD simulation data. The dot shows the mean value based on all simulation replicas, and the line represents the standard deviation. C) The number of hydrogen bonds between nanobody module H11-H4 and the RBD of SARS-CoV-2 VOCs, as predicted by MD simulations. D) The interface between nanobody module H11-H4 (orange) and wild-type RBD (green). E) The interface between nanobody module H11-H4 (orange) and RBD (green) with amino acid change E484K (highlighted in red).

246 For the MR17-K99Y and H11-H4 modules, the R52-E484 salt bridge was identified to be

247 extremely stable throughout the WT simulations and in multiple independent simulation

248 replicas (ca. 95 % of total simulation time). However, when amino acid change E484K was

249 simulated, the interaction to R52 was rapidly broken (within 1 ns). The dissociation of the salt

250 bridge as a consequence of charge change from anionic glutamate to positively charged lysine

251 contributed to higher instability of the E484K RBD, with the surrounding loop becoming more

252 mobile (Figure S2 and S3, Figure 4D-E). In addition, the number of hydrogen bonds between

253 RBD and the nanobody modules decreased in the E484K systems (Figure 4B). The majority of

254 these disrupted hydrogen bonds were identified to be in the conserved RBD binding epitope

255 (Figure 4D-E). Additional model systems were constructed with the full set of VOC mutations

256 in the RBD. Here, the Alpha and Delta VOC, where E484 is preserved, behaved similarly to

257 the WT systems. However, both Beta and Omicron VOC, where E484 is substituted by lysine

258 and alanine respectively, showed higher instability (SI Figure S2) and a decrease in hydrogen

259 bonding interactions throughout the simulation (Figure 4C). These data indicate that E484 is

260 central for strong nanobody binding.

261 **Nanobodies fused to split nanoluciferase fragments detect SARS-CoV-2 Spike at**

262 **picomolar concentrations.** Antibody-based diagnostics are widely used for detecting SARS-

263 CoV-2, as they yield results rapidly and are easy to use in point-of-care and outpatient settings

264 (*40*). Here, we applied nanobody engineering in the development of a novel SARS-CoV-2

265 detection assay. The modular nature of nanobodies makes them amenable to fusion with signal

266 molecules, and their small size allows the targeting of proximal epitopes, such as those

267 presented by the three subunits of the SARS-CoV-2 spike trimer. These properties align well

268 with the principle of protein-fragment complementation assays, where the activity of a split

269 signal molecule, such as a luciferase, a fluorescent protein, or a betalactamase, is restored once

270 the split fragments are brought into close proximity by the interaction of proteins fused to the

271   fragments (*64*). Nanobodies shown in Figure 1 target epitopes in the RBD, and we

272   hypothesized that, when fused to split signal molecule fragments, their binding to the three

273   spike subunits will reconstitute the signal molecule, potentially allowing sensitive detection in

274   a single step.

275   Here, we selected the split version of NanoLuc, an engineered 19-kDa luciferase with enhanced

276   stability and brightness compared to the traditional Renilla and Firefly luciferases (*43, 44*), as

277   the signal molecule for the assay. To create the assay components, RBD-binding nanobody

278   Ty1 (*28*) was fused with fragments of NanoLuc, titled SmBit or LgBit (*42, 44*), using flexible

279    $(GGGGS)_4$ linkers to connect the nanobody monomer and the signal molecule fragments

280   (Figure 5).

281   We performed proof-of-principle experiments to gauge the ability of the nanobody-

282   nanoluciferase fusions to detect recombinantly produced SARS-CoV-2 Spike in solution. 10

283   nM concentrations of each nanobody fusion, one fused to the LgBit and the other to the SmBit

284   fragment, were mixed with a dilution series of either recombinant spike or negative control

285   protein (BSA) and incubated for 15 minutes. The substrate of the nanoluciferase was added

286   immediately before measurement of luminescence from the reactions. The results show that

287   the spike signal can be distinguished from an equimolar concentration of the negative control

288   protein at a concentration as low as 200 pM (Figure 5).

14

289
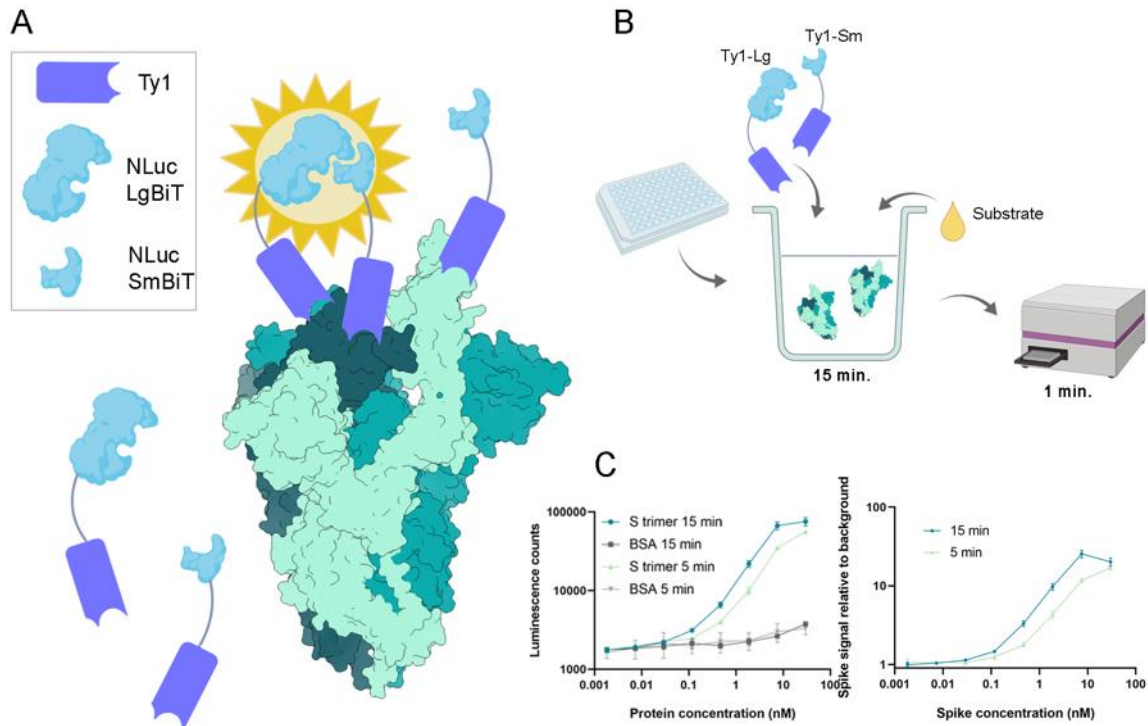
Figure 5. SARS-CoV-2 spike protein detection with a proximity-triggered assay. A) Split nanoluciferase fragments are fused to Ty1 nanobody (*47*) with GGGGS$_4$ linkers. The enzymatic activity of the luciferase is restored upon nanobody binding to adjacent RBDs. B) The reaction setup. The nanobody fusions are added into the wells of an opaque white plate with recombinant spike, and the mixture is incubated for 15 minutes. Then, the substrate is added, and the luminescence reads are recorded from each well. C) and D) The signal caused by spike protein can be distinguished from background down to spike concentration of 200 pM.

298

Discussion

In this study, we created potent SARS-CoV-2 neutralizers and a diagnostic assay through fusions of spike-targeted nanobody modules. Our multimodular nanobodies were linked together with GGGGS$_4$-linkers to facilitate simultaneous binding of the modules to distinct epitopes (Figure 1) and to increase the avidity of binding. We observed a notable increase (up to 100-fold) in the neutralization potency of the multimodular constructs relative to the reported IC50 values of the single constituent nanobodies (SI Table S1) in neutralization assays performed with SARS-CoV-2 wild-type, Alpha, and Delta variants of concern. Multimodular

15

307   nanobodies showed IC50 values in the 50−160 pM range (Figure 3A-B) in cell culture, and, in

308   an animal model, prophylactic administration of tri-TMH in the nasal cavity limited tissue

309   damage in the lungs (Figure 3C).

310   SARS-CoV-2 variants have become the prevalent forms of the virus globally, which warrants

311   that the potency of new neutralizers is validated against these targets. While WT, Alpha, and

312   Delta variants were efficiently neutralized by multimodular nanobodies in this work, Beta and

313   Omicron were significantly less susceptible to neutralization (Figure 3), despite the capability

314   of tri-TMH and tri-TMV nanobodies to bind variant forms of the RBD (Figure 2). This agrees

315   with the previously noted pattern of potent antibodies lacking breadth in SARS-CoV-2

316   neutralization (65).

317   The MD simulations performed in this study indicate that the E484K amino acid change results

318   in a loss of salt bridge with conserved R52 and larger conformational rearrangement in the

319   receptor-binding domain (Figure 4), causing disruption of the nanobody binding interface and

320   leading to the Beta variant escaping neutralization. Notably, the MD simulation data also

321   revealed interaction trends at the antigen interface that correlate well with the experimentally

322   observed neutralization capacity (Figure 3). We postulate that this approach, focused on

323   simulating hydrogen bonding networks and RMSD trends at the antigen interface of emerging

324   variants may be applied to qualitatively predict the potential for escape from specific

325   neutralizers.

326   Drawing from the established field of protein-fragment complementation assays, we were

327   inspired to combine high-affinity nanobody modules with signal molecules to develop new

328   diagnostic tools. Our novel nanobody-based diagnostic assay was successful at detecting low

329   concentrations of SARS-CoV-2 spike protein. This is in line with the limit of detection reported

330   for other antigen test approaches, such as a FRET-based assay (66) and similar to the

16

331   commercially available rapid point-of-care antigen tests (*40*). To our knowledge, this is the

332   first report of a nanobody-based diagnostic approach that makes use of the protein-fragment

333   complementation toolkit. The observed level of detection shows potential for diagnostic use,

334   although future applications would require further validation of the technique with patient

335   samples. In contrast to monoclonal antibodies commonly used in diagnostics, engineered

336   nanobodies have multiple attractive properties, including cheap and scalable production that

337   does not require resource-intensive animal tissue cultures (*51*). It is also becoming feasible to

338   discover nanobodies from synthetic libraries, allowing the transition away from conventional

339   animal immunization prevalent in antibody generation (*67*). Established platforms for the

340   discovery of nanobodies will allow the application of the diagnostic assay presented here to

341   different targets, including viruses emerging in the future. We envision that this combination

342   of nanobody modules with split signal molecules presents a powerful platform for the rapid

343   development of single-step detection assays for emerging pathogens.

344   The COVID-19 pandemic continues, despite substantial efforts to curb the spread of the

345   disease, and emerging variants continue to pose challenges for potential SARS-CoV-2

346   therapeutics. Nanobodies, being inexpensive and readily modified, show great promise as viral

347   inhibitor candidates and diagnostic tools. Exploring the application of engineered nanobodies

348   against viral pathogens will facilitate the development of therapeutics against present and

349   future outbreaks of emerging infectious disease.

350

351   **Materials and Methods**

352   **Production and purification of multimodular and luciferase-fused nanobodies**. The

353   synthetic genes encoding multimodular nanobody constructs and nanobody fusions with split

354   nanoluciferase were obtained as inserts in pET100/D-TOPO vector backbones (GeneArt,

17

355   Thermo Fisher Scientific). Nanobodies were expressed in the bacterial cytoplasm using

356   *Escherichia coli* Rosetta-gami 2 (DE3) cells (Novagen) in autoinduction media. Expression

357   cultures were grown at 37 °C until OD600 reached 0.5, after which the incubation temperature

358   was lowered to 28 °C. The cells were harvested after 24 h from inoculation by centrifugation

359   at $4000 \times g$, 4 °C, for 15 min. The cell pellets were washed by resuspension in PBS. The pellets

360   were flash-frozen in liquid nitrogen and stored at -75 °C until purification.

361   To purify the nanobody constructs, the bacterial cell pellets were resuspended in lysis buffer

362   (10 mM Tris-HCl pH 7.5, 150 mM NaCl). Protease inhibitors and 10 mM imidazole were

363   added to the lysis buffer when purifying the tri-TMH and tri-TMV constructs. Cytoplasmic

364   proteins were extracted by lysing the cell suspension in Emulsiflex C3, and the lysate was

365   clarified by centrifugation at $38\,000 \times g$ for 30 min at 4 °C. The clarified lysate was loaded on

366   a HisTrap FF crude column and washed stepwise with lysis buffer containing 0, 10, 20, 30, and

367   50 mM imidazole, followed by elution with 300 mM imidazole. The eluate was concentrated

368   and buffer-exchanged into lysis buffer to remove imidazole using an Amicon Ultra 15 10K

369   concentrator.

370   To produce an ultrapure nanobody sample, the nanobodies were purified by size-exclusion

371   chromatography (SEC), using the ÄKTA Go system and a Superdex 75 Increase 10/300

372   column. When preparing samples for *in vivo* experiments, sample buffer was exchanged into

373   PBS during SEC. The pooled SEC fractions were further concentrated using an Amicon Ultra

374   10K 0.5 mL concentrator. Buffer-exchanges, when necessary, were performed in the same

375   device.

376   To prepare the nanobodies for neutralization assays, His-tags were removed from the proteins

377   by enterokinase cleavage (Bovine enterokinase, GenScript). Thereafter, the cleaved tags and

378   enzyme were removed from the sample using HisPur Ni-NTA resin (Thermo Scientific) or

379   SEC as described above.

380   **Production and purification of recombinant SARS-CoV-2 S protein.** SARS-CoV-2 spike

381   was expressed from a synthetic cDNA template (GeneArt, Life Technologies) encoding the S

382   protein ectodomain residues 14−1208 from the Wuhan-Hu-1 strain (NCBI Reference

383   Sequence: YP_009724390.1) stabilized in the prefusion state (*4, 7*) with proline substitutions

384   at residues 986 and 987, an abrogated furin S1/S2 cleavage site with a "GSAS" substitution at

385   residues 682–685, and a C-terminal T4 fibritin trimerization motif. In our construct, the

386   trimerization motif was followed by an HRV3C protease cleavage site, SpyTag003 (*68*), and

387   8xHisTag. The gene was cloned into the mammalian expression vector pHLsec (*69*) and

388   transfected into Expi293F™ (Thermo Fisher Scientific) suspension cells at a density of

389   3×10^6 cells per ml using the ExpiFectamine™ 293 Transfection Kit (Thermo Fisher

390   Scientific). Transfected cells were cultivated on an orbital shaker at 36.5 °C and 5% CO2 for

391   six days, after which supernatant was harvested, clarified by centrifugation, filtered through a

392   0.45 µM filter, and supplemented with imidazole to 3 mM final concentration. SARS-CoV-2

393   S-protein was purified from the supernatant by immobilized nickel affinity chromatography

394   with a 1-ml HisTrap excel column (Cytiva) using 300 mM imidazole for elution. The eluate

395   was concentrated and buffer exchanged to 10 mM Tris pH 8 + 150 mM NaCl buffer using an

396   Amicon Ultra centrifugal filter (MWCO 100 kDa, Millipore). Pure S-trimer was used for cryo-

397   EM grid preparation immediately after purification.

398   **Cryo-EM grid preparation, data acquisition and data processing.** A 3-µl aliquot of a pure,

399   prefusion SARS-CoV-2 S-trimer (0.3 mg/ml) mixed with tri-TMH (0.05 mg/ml) was applied

400   on Quantifoil 1.2/1.3 grids (1.2-µm hole diameter, 200 mesh copper) that had been glow

401   discharged in Plasma Cleaner PDC-002-CE (Harrick Plasma) for 30 s. The grids were blotted

19

402   for 6 s and plunged into liquid ethane using a vitrification apparatus (Vitrobot, Thermo Fisher

403   Scientific).

404   Data were collected on a Titan Krios transmission electron microscope (Thermo Fisher

405   Scientific) equipped with Gatan K2 direct electron detector. EPU v 2.11.0 software was used

406   to acquire micrographs, and images were collected with a dose of 1.38 e$^-$/Å² per image (SI

407   Table S2).

408   Data were processed in cryoSPARC (*70*) Movie frames were aligned and averaged to correct

409   for beam induced motion. Contrast transfer function (CTF) parameters were estimated using

410   CTFFIND4 (*71*). An initial set of particles, picked with the blob-picker, was classified and the

411   particles in good 2D classes were used to train Topaz particle picker (*72, 73*). A total of 91,601

412   particles were selected after cleaning the picked set with 2D classification. An initial volume

413   with C3 symmetry was calculated *ab initio*. A consensus map of the S trimer, with C3

414   symmetry applied, was resolved to 2.66-Å resolution. Visual inspection showed that the RBD

415   region was poorly defined in the consensus map. 3D variance analysis or symmetry-expanded

416   particles was run using a spherical mask defining the RBD region, six principal modes (i.e.

417   eigenvectors of the 3D covariance) and eight classes (or clusters). Particles in each class were

418   subjected to local asymmetric refinement (standard deviation over the prior of rotations and

419   shifts were 5 degrees and 5 Å, respectively, centered at the box center). This local refinement

420   prevented symmetry expanded particles from rotating over their symmetry copy. Particles in

421   the cluster corresponding to the "all-down" conformation were subjected to a second round of

422   3D variance analysis using 4 principal modes and 4 classes. Particles from 3 of the 4 classes

423   were combined, symmetry copies removed with the "remove duplicates" function and the map

424   was locally refined with C3 symmetry. Resolution of the maps was estimated based on the

425   gold-standard Fourier shell correlation (FSC) criterion of 0.143 (*74*), and the final maps were

426   filtered to local resolution.

427   Nanobodies were placed in the cryo-EM density maps by docking molecular models of the S

428   trimer (PDB: 7A29) and nanobody-RBD complexes (PDB: 6ZHD, 6ZXN, 7CAN) into the

429   map. First, the "fitmap" function of UCSF Chimera was used to simulate a density for the PDB

430   reference model to the global resolution of each map. The comparison of the simulated maps

431   with corresponding reconstructions by the "fitmap" function yielded correlation scores of

432   0.7269 for the 1-up map and 0.7367 for the all-down map. The "matchmaker" function in

433   UCSF Chimera was used to match models of nanobody-RBD complexes with the RBDs of the

434   full spike model. To account for the mobility of the RBDs, the individual Nb-RBD models

435   were further fitted into the density by the "fitmap" function (correlation scores for Nb-RBD

436   models: 1-up map 0.8064, 0.7843, 0.7824; all-down map 0.7937, 0.7799, 0.8017). This fitting

437   process resulted in nanobodies being placed into the remaining density regions unaccounted

438   for by the spike model.

439   **Proof-of-concept tests for the diagnostic assay with Split NanoLuc-nanobody fusions.** A

440   dilution series was made in triplicate with purified recombinant Spike in Tris buffer (10 mM

441   Tris-HCl pH 7.5, 150 mM NaCl). In each well, purified Ty1-LgBiT and Ty1-SmBiT constructs

442   were added at 10 nM final concentration each. In parallel, an equimolar dilution series of

443   bovine serum albumin was identically treated with the nanobody constructs to determine the

444   signal-to-noise ratio in the luminescence reaction. The mixture was incubated for 15 minutes

445   at room temperature, after which the nanoluciferase substrate coelenterazine H was mixed into

446   the sample at 200 nM final concentration. Immediately following substrate addition, the

447   luminescence readings were measured with Perkin-Elmer EnSpire multimode plate reader,

448   using the 'Luminescence' program. To calculate the final luminescence measurement while

449   taking noise into account, the average readings of each triplicate sample were divided with

450   corresponding averages from the BSA dilutions.

21

451 **Labelling of nanobodies with DyLight 633.** The nanobodies were labelled with DyLight 633

452 in PBS supplemented with 50 mM sodium borate (pH 8.5) at 1 mg/mL protein concentration

453 and 50 µM Dylight 633 NHS ester (Thermo Fischer Scientific) at room temperature for 2h,

454 followed by removal of unreacted dye with Zeba Spin 7K MWCO desalting columns (Thermo

455 Scientific).

456 **Antigen array.** Wild type and variant SARS-CoV-2 RBD and Spike S1 domains were

457 biotinylated and arrayed as duplicate spots (0.1 ng per spot) in the wells of streptavidin-coated

458 microtitration plates using a piezoelectric non-contact microarray dispenser (Nano-Plotter,

459 GeSiM, Germany). The antigens were purchased from the following sources: RBD wt (aa 319-

460 541 of the S protein) and S1 wt (aa 14-681 of the S protein) from Medix Biochemica; RBD

461 single mutants K417N, E484K and N501Y and S1(K417N, E484K, N501Y, D614G)

462 quadruple mutant from SinoBiological.

463 **Binding assays on antigen array.** The antigen arrays in microplate wells were blocked with

464 50 µL of Assay buffer (Tris-buffered saline (TBS), pH 8.0 + 0.05% Tween 20) per well for 30

465 min at RT, followed by three washes with Washing buffer (TBS containing 0.05% Tween 20).

466 DyLight 633 -labelled nanobody solutions (1 µg/mL in Assay buffer) were added 50 µL/well,

467 incubated in a plate shaker at 600 rpm, RT for 1h, followed by three washes with Washing

468 buffer. Residual liquid droplets were removed by centrifuging the plate upside down on a paper

469 towel in a plate adapter (453 g, 1 min), after which the plate was let dry for 15 min in a 37°C

470 room. The Dylight 633 -labelled nanobodies bound to the arrayed antigens were detected by

471 fluorescence scanning through the clear bottom of the microplate with a Tecan LS400 confocal

472 laser scanner, using a 633 nm laser for excitation and a 670/25 emission filter.

473 The fluorescence scan images were analyzed with Array-Pro Analyzer software (Media

474 Cybernetics) and the raw spot signal data was exported to Microsoft Excel for further

475 calculations. Net signals were obtained by subtracting the well background from the raw spot

476 signals (average pixel intensity in the spot area), after which the spot signals were normalized

477 to the wild type antigen spot signals in the same well: single RBD mutant signals were

478 expressed as percentage of the RBD wt signal whereas the quadruple S1 mutant signal was

479 expressed as percentage of the S1 wt signal.

480 **Neutralization assays**. VeroE6-TMPRSS2-H10 cells (*66*) were seeded to 96-well plates

481 (white-sided optically clear bottom PerkinElmer) in density 30 000 cells/well 24 h before the

482 assay. The nanobodies were diluted in series 1:150 000, 1:300 000, 1:600 000, 1:1 200 000,

483 1:1 240 000, and 1:4 800 000 in virus growth medium (VGM) containing MEM (Sigma, 2279),

484 2 % FBS, L-glutamine, and 1x penicillin-streptomycin. Diluted nanobodies were mixed with

485 the 50 pfu (Figure 3) or MOI 1 (SI Figure S5) (for wild-type, Alpha, Beta, and Delta) or MOI

486 0.2 (for Omicron) virus and incubated for 1 h at 37°C 5% CO_2. Thereafter, the cells were treated

487 with the mixture of the nanobodies and the virus. The virus dilution in VGM without the

488 nanobodies was used as a negative control and non-infected cells (MOCK) was used as a

489 positive control of the nanobody neutralization effectiveness. After 5 days of incubation the

490 medium was removed, and cells were treated with CellTiter-Glo 2.0 cell viability assay reagent

491 (Promega, G9243) for 20 min at RT. Then, the cellular ATP was measured via the detection of

492 luminescent signal using HIDEX Sence microplate reader (Hidex Oy, Finland) Viability of the

493 MOCK infected cells was considered as 100 %. Neutralization efficacy percentage for each

494 measurement was calculated considering MOCK infected cells as 100% neutralization and

495 untreated, virus infected cells as 0% neutralization. Curve-fitting and IC50 calculation was

496 performed for the normalized neutralization data with GraphPad Prism version 9.2.0 for

497 Windows, using the Nonlinear regression method (Absolute IC50, X is concentration), with

498 baseline constraint set to zero.

499   **Animal experiments.** A total of 20 male and female Syrian Golden hamsters were obtained

500   from (Scanbur, Karl Sloanestran, Denmark), moved to the University of Helsinki biosafety

501   level-3 (BSL-3) facility and allowed to acclimatize to individually ventilated biocontainment

502   cages (ISOcage; Scanbur, Karl Sloanestran, Denmark) for seven days with ad libitum water

503   and food (rodent pellets) prior to infection.

504   For the main experiment, six 8-week-old male and female Syrian Golden hamsters received 30

505   µg of nanobody, in 0.61 mg/mL concentration, 6 h prior to intranasal infection with 5×10^4

506   SARS-CoV-2 (wt/D614G strain). The control group received an equal volume of PBS (n = 4).

507   Euthanasia was performed under terminal isoflurane anaesthesia with cervical dislocation and

508   were dissected immediately after death. Samples were collected from the lungs for RT-qPCR

509   and the remaining lung tissue including trachea, heart, oesophagus and bronchial lymph nodes

510   were immersed in 10% buffered formalin. After 48 h, the tissue was transferred to and stored

511   in 70% ethanol until processing for histological and immunohistological examination.

512   **RT-qPCR.** RNA was extracted from lung samples using Trizol (Thermo Scientific) according

513   to the manufacturers' instructions. Isolated RNA was directly subjected to one-step RT-qPCR

514   analysis based on a previously described protocol for RdRp (*75*) and for E and subE genes (*76*)

515   with TaqMan fast virus 1-step master mix (Thermo Scientific) using AriaMx instrumentation

516   (Agilent, Santa Clara, CA, USA). The actin RT-qPCR used for normalization is described in

517   (*77*). Fold differences between samples were calculated by the comparative Ct method (*78*)

518   using the average of normalized Ct values from non-nanobody treated infected animal lung

519   tissues as reference.

520   **Histological, immunohistological and morphometrical analyses.** Three to five cross

521   sections were prepared from the fixed lung tissue and routinely paraffin wax embedded.

522   Consecutive sections (3-5 µm) were prepared and stained with hematoxylin eosin (HE) for

24

523 histological examination or subjected to immunohistological staining for SARS-CoV-2 antigen

524 expression, using a previously published staining protocol (*79*). For immunohistology, the

525 horseradish peroxidase method was applied. Rabbit anti-SARS-CoV nucleocapsid protein

526 (Rockland, 200-402-A50) served as the primary antibody, and DAB (EnVision FLEX DAB+

527 Chromogen in Substrate buffer; Agilent) for visualization of antibody binding. All incubations

528 took place in an autostainer (Dako). Sections were subsequently counterstained with

529 haematoxylin.

530 For morphometric analysis, the immunostained sections were scanned (NanoZoomer-XR

531 C12000; Hamamatsu, Hamamatsu City, Japan) and analysed using the software programme

532 Visiopharm (Visiopharm 2020.08.1.8403; Visiopharm, Hoersholm, Denmark) to quantify the

533 area of viral antigen expression in relation to the total area (= area occupied by lung

534 parenchyma) in the sections. This was used to compare the extent of viral antigen expression

535 in the lungs between untreated and treated animals. A first app was applied that outlined the

536 entire lung tissue as ROI (total area). For this a Decision Forest method was used and the

537 software was trained to detect the lung tissue section (total area). Once the lung section was

538 outlined as ROI the lumen of large bronchi and vessels was manually excluded from the ROI.

539 Subsequently, a second app with Decision Forest method was trained to detect viral antigen

540 expression (as brown DAB precipitate) within the ROI.

541 **Molecular dynamics simulations of nanobody-RBD interface.** MD simulations were

542 performed on the model systems constructed using the cryo-EM structure of nanobody

543 monomers and RBD (PDB 6ZXN, 7CAN, 6ZBP). During model system construction long

544 glycine linkers were removed. VMD psfgen tool (*80*) was employed to add missing hydrogen

545 atoms, make point mutations, and solvate the systems with TIP3P water and 0.1 M NaCl to

546 give a total system size of ca. 150,000 atoms. The force field for all components of the system

547 was CHARMM36 (*81*). GROMACS v20.3 (*82*) was used for all equilibration and production

548   simulations. First, the initial systems were minimized with restraints on heavy protein atoms

549   (20,000 kJ mol^{-1} nm^{-2}). Following convergence, a 100 ps NVT equilibration was performed

550   with the same restraints, followed by a 10 ns NPT with the restraints only on the protein

551   backbone atoms. All restraints were removed for the production runs, which employed the

552   LINCS algorithm (*83*) to achieve a 2 fs timestep and used the Nosé -Hoover thermostat (*84,*

553   *85*) to maintain 310 K temperature and the Parrinello-Rahman barostat (*86*) to maintain 1 atm

554   pressure. The electrostatic interactions were controlled by the particle mesh Ewald method (*87*)

555   with a 12 Å cutoff, while the van der Waals cutoff was also 12 Å, with a switching distance of

556   10 Å. Multiple independent simulation replicas were performed and trajectories were

557   visualized and analyzed using VMD (*80*) and Pymol (The PyMOL Molecular Graphics System,

558   Version 1.2r3pre, Schrödinger, LLC). **Table S3** lists system setups and their respective lengths.

559   **Molecular graphics.** Molecular graphics images were generated using PyMOL (The PyMOL

560   Molecular Graphics System, Version 2.4.0a0, Schrödinger, LLC), UCSF Chimera (*88*), and

561   UCSF ChimeraX (*89*).

562   **Protein interface analysis.** Residues comprising the epitopes of nanobody modules Ty1 (PDB

563   6ZXN), H11-H4 (PDB 6ZH9), MR17-K99Y (PDB 7CAN) and VHH V (PDB 7KN6) on

564   SARS-CoV-2 S were identified using the PDB ePISA server (*90*).

565

580   **Competing interests statement**. The authors declare no competing interest.

References

1. B. D. Kevadiya *et al.*, Diagnostics for SARS-CoV-2 infections. *Nat Mater* **20**, 593-605 (2021). 10.1038/s41563-020-00906-z

2. Y. C. Hwang *et al.*, Monoclonal antibodies for COVID-19 therapy and SARS-CoV-2 detection. *J Biomed Sci* **29**, 1 (2022). 10.1186/s12929-021-00784-w

3. A. Torrente-Lopez *et al.*, The Relevance of Monoclonal Antibodies in the Treatment of COVID-19. *Vaccines (Basel)* **9**, (2021). 10.3390/vaccines9060557

4. A. C. Walls *et al.*, Structure, Function, and Antigenicity of the SARS-CoV-2 Spike Glycoprotein. *Cell* **181**, 281-292.e286 (2020). 10.1016/j.cell.2020.02.058

5. C. O. Barnes *et al.*, Structures of Human Antibodies Bound to SARS-CoV-2 Spike Reveal Common Epitopes and Recurrent Features of Antibodies. *Cell* **182**, 828-842 (2020). 10.1016/j.cell.2020.06.025

6. M. Hoffmann *et al.*, SARS-CoV-2 Cell Entry Depends on ACE2 and TMPRSS2 and Is Blocked by a Clinically Proven Protease Inhibitor. *Cell* **181**, 271-280.e278 (2020). 10.1016/j.cell.2020.02.052

7. D. Wrapp *et al.*, Cryo-EM structure of the 2019-nCoV spike in the prefusion conformation. **367**, 1260-1263 (2020). 10.1126/science.abb2507

8. R. Yan *et al.*, Structural basis for the recognition of SARS-CoV-2 by full-length human ACE2. *Science* **367**, 1444-1448 (2020). 10.1126/science.abb2762

9. J. Shang *et al.*, Structural basis of receptor recognition by SARS-CoV-2. *Nature* **581**, 221-224 (2020). 10.1038/s41586-020-2179-y

10. M. Hoffmann, H. Kleine-Weber, S. Pohlmann, A Multibasic Cleavage Site in the Spike Protein of SARS-CoV-2 Is Essential for Infection of Human Lung Cells. *Mol Cell* **78**, 779-784.e775 (2020). 10.1016/j.molcel.2020.04.022

605   11.   K. Subbarao, The success of SARS-CoV-2 vaccines and challenges ahead. *Cell Host*

606   *Microbe* **29**, 1111-1123 (2021). 10.1016/j.chom.2021.06.016

607   12.   Y. Weisblum *et al.*, Escape from neutralizing antibodies by SARS-CoV-2 spike protein

608   variants. *Elife* **9**, e61312 (2020). 10.7554/eLife.61312

609   13.   Y. Zhang, J. L. Banga Ndzouboukou, M. Gan, X. Lin, X. Fan, Immune Evasive Effects

610   of SARS-CoV-2 Variants to COVID-19 Emergency Used Vaccines. *Front Immunol*

611   **12**, 771242 (2021). 10.3389/fimmu.2021.771242

612   14.   T. Tada *et al.*, Increased resistance of SARS-CoV-2 Omicron variant to neutralization

613   by vaccine-elicited and therapeutic antibodies. *EBioMedicine* **78**, 103944 (2022).

614   10.1016/j.ebiom.2022.103944

615   15.   P. Supasa *et al.*, Reduced neutralization of SARS-CoV-2 B.1.1.7 variant by

616   convalescent   and   vaccine   sera.   *Cell*   **184**,   2201-2211.e2207   (2021).

617   10.1016/j.cell.2021.02.033

618   16.   D. Zhou *et al.*, Evidence of escape of SARS-CoV-2 variant B.1.351 from natural and

619   vaccine-induced sera. *Cell* **184**, 2348-2361.e2346 (2021). 10.1016/j.cell.2021.02.037

620   17.   H. Tegally *et al.*, Detection of a SARS-CoV-2 variant of concern in South Africa.

621   *Nature* **592**, 438-443 (2021). 10.1038/s41586-021-03402-9

622   18.   N. G. Davies *et al.*, Estimated transmissibility and impact of SARS-CoV-2 lineage

623   B.1.1.7 in England. *Science* **372**, eabg3055 (2021). 10.1126/science.abg3055

624   19.   P. Mlcochova *et al.*, SARS-CoV-2 B.1.617.2 Delta variant replication and immune

625   evasion. *Nature* **599**, 114-119 (2021). 10.1038/s41586-021-03944-y

626   20.   Y. Cao *et al.*, Humoral immune response to circulating SARS-CoV-2 variants elicited

627   by   inactivated   and   RBD-subunit   vaccines.   *Cell Res* **31**, 732-741 (2021).

628   10.1038/s41422-021-00514-9

629   21.   A. Tuekprakhon *et al.*, Antibody escape of SARS-CoV-2 Omicron BA.4 and BA.5 from

630   vaccine   and   BA.1   serum.   *Cell*   **185**,   2422-2433.e2413   (2022).

631   10.1016/j.cell.2022.06.005

632   22.   W. B. Wang *et al.*, E484K mutation in SARS-CoV-2 RBD enhances binding affinity

633   with hACE2 but reduces interactions with neutralizing antibodies and nanobodies:

634   Binding free energy calculation studies. *J Mol Graph Model* **109**, 108035 (2021).

635   10.1016/j.jmgm.2021.108035

636   23.   A. Baum *et al.*, Antibody cocktail to SARS-CoV-2 spike protein prevents rapid

637   mutational escape seen with individual antibodies. *Science* **369**, 1014-1018 (2020).

638   10.1126/science.abd0831

639   24.   Y. Kakinoki *et al.*, Impact of Antibody Cocktail Therapy Combined with Casirivimab

640   and Imdevimab on Clinical Outcome for patients with COVID-19 in A Real-Life

641   Setting: A Single Institute Analysis. *Int J Infect Dis* **117**, 189-194 (2022).

642   10.1016/j.ijid.2022.01.067

643   25.   F. D. Mast *et al.*, Highly synergistic combinations of nanobodies that target SARS-

644   CoV-2 and are resistant to escape. *eLife* **10**, e73027 (2021). 10.7554/eLife.73027

645   26.   Y. Wang *et al.*, Nanobody-derived nanobiotechnology tool kits for diverse biomedical

646   and biotechnology applications. *International Journal of Nanomedicine* **11**, 3287-3303

647   (2016). 10.2147/IJN.S107194

648   27.   S. Nambulli *et al.*, Inhalable Nanobody (PiN-21) prevents and treats SARS-CoV-2

649   infections in Syrian hamsters at ultra-low doses. *Science Advances* **7**, eabh0319 (2021).

650   10.1126/sciadv.abh0319

651   28.   L. Hanke *et al.*, An alpaca nanobody neutralizes SARS-CoV-2 by blocking receptor

652   interaction. *Nature Communications* **11**, 1-9 (2020). 10.1038/s41467-020-18174-5

30

653   29.   J. Huo *et al.*, Neutralizing nanobodies bind SARS-CoV-2 spike RBD and block

654   interaction with ACE2. *Nature Structural and Molecular Biology* **27**, 846-854 (2020).

655   10.1038/s41594-020-0469-6

656   30.   T. Li *et al.*, A synthetic nanobody targeting RBD protects hamsters from SARS-CoV-

657   2 infection. *Nat Commun* **12**, 4635 (2021). 10.1038/s41467-021-24905-z

658   31.   D. Wrapp *et al.*, Structural Basis for Potent Neutralization of Betacoronaviruses by

659   Single-Domain Camelid Antibodies. *Cell* **181**, 1004-1015.e1015 (2020).

660   10.1016/j.cell.2020.04.031

661   32.   P. Pymm *et al.*, Nanobody cocktails potently neutralize SARS-CoV-2 D614G N501Y

662   variant and protect mice. *Proc Natl Acad Sci U S A* **118**, e2101918118 (2021).

663   10.1073/pnas.2101918118

664   33.   H. Ma *et al.*, Potent Neutralization of SARS-CoV-2 by Hetero-bivalent Alpaca

665   Nanobodies Targeting the Spike Receptor-Binding Domain. *J Virol* **95**, e02438-02420

666   (2021). 10.1128/JVI.02438-20

667   34.   G. Valenzuela Nieto *et al.*, Potent neutralization of clinical isolates of SARS-CoV-2

668   D614 and G614 variants by a monomeric, sub-nanomolar affinity nanobody. *Scientific*

669   *Reports* **11**, 3318-3318 (2021). 10.1038/s41598-021-82833-w

670   35.   J. Xu *et al.*, Nanobodies from camelid mice and llamas neutralize SARS-CoV-2

671   variants. *Nature* **595**, 278-282 (2021). 10.1038/s41586-021-03676-z

672   36.   J. Dong *et al.*, Development of multi-specific humanized llama antibodies blocking

673   SARS-CoV-2/ACE2 interaction with high affinity and avidity. *Emerging Microbes &*

674   *Infections* **9**, 1034-1036 (2020). 10.1080/22221751.2020.1768806

675   37.   T. J. Esparza, N. P. Martin, G. P. Anderson, E. R. Goldman, D. L. Brody, High affinity

676   nanobodies block SARS-CoV-2 spike receptor binding domain interaction with human

677   angiotensin converting enzyme. *Scientific Reports* **10**, (2020). 10.1038/s41598-020-

678   79036-0

679 38. A. Hultberg *et al.*, Llama-derived single domain antibodies to build multivalent,

680   superpotent and broadened neutralizing anti-viral molecules. *PLoS One* **6**, e17665

681   (2011). 10.1371/journal.pone.0017665

682 39. C. Palomo *et al.*, Trivalency of a Nanobody Specific for the Human Respiratory

683   Syncytial Virus Fusion Glycoprotein Drastically Enhances Virus Neutralization and

684   Impacts Escape Mutant Selection. *Antimicrob Agents Chemother* **60**, 6498-6509

685   (2016). 10.1128/AAC.00842-16

686 40. V. M. Corman *et al.*, Comparison of seven commercial SARS-CoV-2 rapid point-of-

687   care antigen tests: a single-centre laboratory evaluation study. *The Lancet Microbe* **2**,

688   e311-e319 (2021). 10.1016/s2666-5247(21)00056-2

689 41. P.-A. Koenig, F. I. Schmidt, Structure-guided multivalent nanobodies block SARS-

690   CoV-2 infection and suppress mutational escape. *Science* **6230**, 6-6 (2021).

691 42. M. P. Hall *et al.*, Engineered luciferase reporter from a deep sea shrimp utilizing a novel

692   imidazopyrazinone   substrate.   *ACS   Chem   Biol*   **7**,   1848-1857   (2012).

693   10.1021/cb3002478

694 43. C. G. England, E. B. Ehlerding, W. Cai, NanoLuc: A Small Luciferase Is Brightening

695   Up   the   Field   of   Bioluminescence.   *Bioconjug Chem*   **27**,   1175-1187   (2016).

696   10.1021/acs.bioconjchem.6b00112

697 44. Y. Ohmuro-Matsuyama, H. Ueda, in *Bioluminescence - Analytical Applications and*

698   *Basic Biology*. (IntechOpen, 2019).

699 45. P. J. M. Brouwer *et al.*, Potent neutralizing antibodies from COVID-19 patients define

700   multiple   targets   of   vulnerability.   *Science*   **369**,   643-650   (2020).

701   10.1126/science.abc5902

702 46. B. Ju *et al.*, Human neutralizing antibodies elicited by SARS-CoV-2 infection. *Nature*
703   **584**, 115-119 (2020). 10.1038/s41586-020-2380-z

704 47. L. Hanke *et al.*, An alpaca nanobody neutralizes SARS-CoV-2 by blocking receptor
705   interaction. *Nat Commun* **11**, 4420 (2020). 10.1038/s41467-020-18174-5

706 48. L. Cao *et al.*, De novo design of picomolar SARS-CoV-2 miniprotein inhibitors.
707   *Science* **370**, 426-431 (2020). 10.1126/science.abd9909

708 49. Y. Cai *et al.*, Distinct conformational states of SARS-CoV-2 spike protein. *Science* **369**,
709   1586-1592 (2020). 10.1126/science.abd4251

710 50. R. Henderson *et al.*, Controlling the SARS-CoV-2 spike glycoprotein conformation.
711   *Nat Struct Mol Biol* **27**, 925-933 (2020). 10.1038/s41594-020-0479-4

712 51. S. Steeland, R. E. Vandenbroucke, C. Libert, Nanobodies as therapeutics: big
713   opportunities for small antibodies. *Drug Discov Today* **21**, 1076-1113 (2016).
714   10.1016/j.drudis.2016.04.003

715 52. T. Chanier, P. Chames, Nanobody Engineering: Toward Next Generation
716   Immunotherapies and Immunoimaging of Cancer. *Antibodies (Basel)* **8**, 13 (2019).
717   10.3390/antib8010013

718 53. A. Desmyter *et al.*, Neutralization of Human Interleukin 23 by Multivalent Nanobodies
719   Explained by the Structure of Cytokine-Nanobody Complex. *Front Immunol* **8**, 884
720   (2017). 10.3389/fimmu.2017.00884

721 54. J. Lan *et al.*, Structure of the SARS-CoV-2 spike receptor-binding domain bound to the
722   ACE2 receptor. *Nature* **581**, 215-220 (2020). 10.1038/s41586-020-2180-5

723 55. P. Wang *et al.*, Antibody resistance of SARS-CoV-2 variants B.1.351 and B.1.1.7.
724   *Nature* **593**, 130-135 (2021). 10.1038/s41586-021-03398-2

725 56. D. Planas *et al.*, Sensitivity of infectious SARS-CoV-2 B.1.1.7 and B.1.351 variants to
726   neutralizing antibodies. *Nat Med* **27**, 917-924 (2021). 10.1038/s41591-021-01318-5

727 57. M. Schoof *et al.*, An ultrapotent synthetic nanobody neutralizes SARS-CoV-2 by
728   stabilizing inactive Spike. *Science* **3255**, eabe3255-eabe3255 (2020).
729   10.1126/science.abe3255

730 58. Y. Xiang *et al.*, Versatile and multivalent nanobodies efficiently neutralize SARS-CoV-
731   2. *Science* **4747**, eabe4747-eabe4747 (2020). 10.1126/science.abe4747

732 59. X. Deng *et al.*, Transmission, infectivity, and neutralization of a spike L452R SARS-
733   CoV-2 variant. *Cell* **184**, 3426-3437 e3428 (2021). 10.1016/j.cell.2021.04.025

734 60. Z. Ke *et al.*, Structures and distributions of SARS-CoV-2 spike proteins on intact
735   virions. *Nature* **588**, 498-502 (2020). 10.1038/s41586-020-2665-2

736 61. J. Huo *et al.*, Neutralization of SARS-CoV-2 by Destruction of the Prefusion Spike.
737   *Cell Host Microbe* **28**, 445-454 e446 (2020). 10.1016/j.chom.2020.06.010

738 62. T. Li *et al.*, Cross-neutralizing antibodies bind a SARS-CoV-2 cryptic site and resist
739   circulating variants. *Nat Commun* **12**, 5652 (2021). 10.1038/s41467-021-25997-3

740 63. Z. Cui *et al.*, Structural and functional characterizations of infectivity and immune
741   evasion of SARS-CoV-2 Omicron. *Cell* **185**, 860-871 e813 (2022).
742   10.1016/j.cell.2022.01.019

743 64. E. Blaszczak, N. Lazarewicz, A. Sudevan, R. Wysocki, G. Rabut, Protein-fragment
744   complementation assays for large-scale analysis of protein-protein interactions.
745   *Biochem Soc Trans* **49**, 1337-1348 (2021). 10.1042/BST20201058

746 65. C. Dacon *et al.*, Broadly neutralizing antibodies target the coronavirus fusion peptide.
747   *Science* **377**, 728-735 (2022). doi:10.1126/science.abq3773

748 66. J. Rusanen *et al.*, A Generic, Scalable, and Rapid Time-Resolved Förster Resonance
749   Energy Transfer-Based Assay for Antigen Detection - SARS-CoV-2 as a Proof of
750   Concept. *mBio* **12**, e00902-00921 (2021). doi:10.1128/mBio.00902-21

751 67. S. Muyldermans, Applications of Nanobodies. *Annu Rev Anim Biosci* **9**, 401-421

752   (2021). 10.1146/annurev-animal-021419-083831

753 68. A. H. Keeble *et al.*, Approaching infinite affinity through engineering of peptide-

754   protein interaction. *Proc Natl Acad Sci U S A* **116**, 26523-26533 (2019).

755   10.1073/pnas.1909653116

756 69. A. R. Aricescu, W. Lu, E. Y. Jones, A time- and cost-efficient system for high-level

757   protein production in mammalian cells. *Acta Crystallogr D Biol Crystallogr* **62**, 1243-

758   1250 (2006). 10.1107/S0907444906029799

759 70. A. Punjani, J. L. Rubinstein, D. J. Fleet, M. A. Brubaker, cryoSPARC: algorithms for

760   rapid unsupervised cryo-EM structure determination. *Nat Methods* **14**, 290-296 (2017).

761   10.1038/nmeth.4169

762 71. A. Rohou, N. Grigorieff, CTFFIND4: Fast and accurate defocus estimation from

763   electron micrographs. *J Struct Biol* **192**, 216-221 (2015). 10.1016/j.jsb.2015.08.008

764 72. T. Bepler, K. Kelley, A. J. Noble, B. Berger, Topaz-Denoise: general deep denoising

765   models for cryoEM and cryoET. *Nat Commun* **11**, 5208 (2020). 10.1038/s41467-020-

766   18952-1

767 73. T. Bepler *et al.*, Positive-unlabeled convolutional neural networks for particle picking

768   in cryo-electron micrographs. *Nat Methods* **16**, 1153-1160 (2019). 10.1038/s41592-

769   019-0575-8

770 74. S. H. Scheres, S. Chen, Prevention of overfitting in cryo-EM structure determination.

771   *Nat Methods* **9**, 853-854 (2012). 10.1038/nmeth.2115

772 75. V. M. Corman *et al.*, Detection of 2019 novel coronavirus (2019-nCoV) by real-time

773   RT-PCR. *Euro Surveill* **25**, (2020). 10.2807/1560-7917.ES.2020.25.3.2000045

35

774   76.   G. Dagotto *et al.*, Comparison of Subgenomic and Total RNA in SARS-CoV-2-
775   Challenged Rhesus Macaques. *Journal of Virology* **95**, e02370-02320 (2021).
776   doi:10.1128/JVI.02370-20

777   77.   M. Zivcec, D. Safronetz, E. Haddock, H. Feldmann, H. Ebihara, Validation of assays
778   to monitor immune responses in the Syrian golden hamster (Mesocricetus auratus). *J
779   Immunol Methods* **368**, 24-35 (2011). 10.1016/j.jim.2011.02.004

780   78.   T. D. Schmittgen, K. J. Livak, Analyzing real-time PCR data by the comparative CT
781   method. *Nature Protocols* **3**, 1101-1108 (2008). 10.1038/nprot.2008.73

782   79.   J. Huo *et al.*, A potent SARS-CoV-2 neutralising nanobody shows therapeutic efficacy
783   in the Syrian golden hamster model of COVID-19. *Nature Communications* **12**, (2021).
784   10.1038/s41467-021-25480-z

785   80.   W. Humphrey, A. Dalke, K. Schulten, VMD: Visual molecular dynamics. *Journal of
786   Molecular Graphics* **14**, 33-38 (1996). https://doi.org/10.1016/0263-7855(96)00018-5

787   81.   A. D. MacKerell *et al.*, All-Atom Empirical Potential for Molecular Modeling and
788   Dynamics Studies of Proteins. *The Journal of Physical Chemistry B* **102**, 3586-3616
789   (1998). 10.1021/jp973084f

790   82.   M. J. Abraham *et al.*, GROMACS: High performance molecular simulations through
791   multi-level parallelism from laptops to supercomputers. *SoftwareX* **1-2**, 19-25 (2015).
792   https://doi.org/10.1016/j.softx.2015.06.001

793   83.   B. Hess, P-LINCS: A Parallel Linear Constraint Solver for Molecular Simulation.
794   *Journal of Chemical Theory and Computation* **4**, 116-122 (2008). 10.1021/ct700200b

795   84.   W. G. Hoover, Canonical dynamics: Equilibrium phase-space distributions. *Physical
796   Review A* **31**, 1695-1697 (1985). 10.1103/PhysRevA.31.1695

797   85.   S. Nosé, A unified formulation of the constant temperature molecular dynamics
798   methods. *The Journal of Chemical Physics* **81**, 511-519 (1984). 10.1063/1.447334

36

799   86.   M. Parrinello, A. Rahman, Polymorphic transitions in single crystals: A new molecular

800   dynamics method. *Journal of Applied Physics* **52**, 7182-7190 (1981). 10.1063/1.328693

801   87.   T. Darden, D. York, L. Pedersen, Particle mesh Ewald: An N·log(N) method for Ewald

802   sums in large systems. *The Journal of Chemical Physics* **98**, 10089-10092 (1993).

803   10.1063/1.464397

804   88.   E. F. Pettersen *et al.*, UCSF Chimera--a visualization system for exploratory research

805   and analysis. *Journal of computational chemistry* **25**, 1605-1612 (2004).

806   10.1002/jcc.20084

807   89.   E. F. Pettersen *et al.*, UCSF ChimeraX: Structure visualization for researchers,

808   educators, and developers. *Protein Sci* **30**, 70-82 (2021). 10.1002/pro.3943

809   90.   E. Krissinel, K. Henrick, Inference of macromolecular assemblies from crystalline

810   state. *J Mol Biol* **372**, 774-797 (2007). 10.1016/j.jmb.2007.05.022

811